PAPER

Check for updates

Recognizing soft templates as stimulators in multivariate modulation of tin phosphate and its application in catalysis for alkyl levulinate synthesis†

Pandian Manjunathan, [iD] [ab] Dhanush Y. Shanbhag,[c] Ajayan Vinu [iD] [c] and Ganapati V. Shanbhag [iD] *[a]

Catalyst synthesis is an art where an inefficient material can be remarkably converted into a highly active and selective catalyst by adopting a suitable synthetic strategy to tune its properties during synthesis. The underlying principle of the strategy presented here is the integration of tailoring the structural and chemical behavior of tin phosphates with tuned catalytic active centers directed by employing different structure directing agents (SDAs) and the attempt to understand this in detail. It is demonstrated how soft templates can be effectively used for their so far unknown utilization of tuning the active sites in phosphate containing catalysts. We found that, by using an appropriate synthesis strategy, it is possible to tune and control explicitly both the catalyst morphology and the nature of active sites at the same time. The ^{31}P MAS NMR study revealed that employing SDAs in the synthesis strongly influenced the nature and amount of phosphate species in addition to porosity. The resultant different nanostructured SnPO catalysts were investigated for one-pot synthesis of alkyl levulinates *via* alcoholysis of furfuryl alcohol. Among the catalysts, SnPO-P123 exhibited greater butyl levulinate yield *via* alcoholysis of furfuryl alcohol with *n*-butanol and the study was extended to synthesize different alkyl levulinates. Importantly, the active sites in the SnPO-P123 catalyst responsible for the reaction were elucidated by a study using 2,6-lutidine as a basic probe molecule. This study therefore provides an avenue for rational design and construction of highly efficient and robust nanostructured SnPO catalysts to produce alkyl levulinates selectively.

Introduction

Metal phosphates as phosphorus-based catalytic materials have been reported for acid catalysis to produce chemicals.[1–5] Metal phosphates, like AlPOs, contain a metal and P in the framework structure joined by oxygen atoms. Materials with a pore size ranging between 2 and 50 nm are known as mesoporous materials and they exhibit versatile applications due to the presence of a high surface area, tunable pore size and their diverse frameworks.[6–10] Metal phosphates exhibit acidic properties and additionally the presence of mesopores helps in improving their efficiency as a solid catalyst. Mesoporous metal phosphates have been previously employed as efficient catalysts for acid catalyzed reactions owing to the presence of a large surface area, porosity and acidity.[11–15]

Tin phosphates, a class of metal phosphates composed of tin and phosphorus in the framework connected through an oxygen bridge, display excellent thermal and chemical behavior. Mesoporous tin phosphates (SnPOs) have been employed as catalysts in a few reactions such as the dehydration of carbohydrates and glucose into 5-hydroxymethylfurfural,[4,5] propan-2-ol decomposition[16] and the production of lactic acid from triose sugars.[17,18] Though tin phosphate is catalytically active, its structural and chemical properties have not been well understood so far. Indeed, multivariate modulation of solid catalysts by tailoring of structural and chemical properties to enhance catalytic performance is a challenging task. In this context, inspired by the benefit of structure directing agents in nanostructured material synthesis and with our goal of tailoring the

[a] Materials Science and Catalysis Division, Poornaprajna Institute of Scientific Research (PPISR), Bidalur Post, Devanahalli, Bengaluru-562164, Karnataka, India. E-mail: shanbhag@poornaprajna.org
[b] Graduate Studies, Manipal Academy of Higher Education, Manipal-576104, Karnataka, India
[c] Global Innovative Center for Advanced Nanomaterials (GICAN), Faculty of Engineering and Built Environment, The University of Newcastle, Callaghan, NSW 2308, Australia

† Electronic supplementary information (ESI) available: Experimental section, powder XRD patterns, nitrogen sorption isotherm, BJH pore size distribution, pyridine-FTIR, NH$_3$-TPD profile, EDS, SEM image, mass spectra, FTIR spectra and additional catalytic activity results are given in the ESI. See DOI: 10.1039/d0cy01637c

multivariate properties of tin phosphate to improve its catalytic properties in acid-catalyzed reactions, we tuned the material properties by adopting different strategies during the synthesis and use of a suitable structure directing agent (SDA, soft template) to control the pore size, particle growth and other physico-chemical properties. The catalytic properties of the tailored tin phosphates were investigated towards a challenging biomass reaction for one-pot synthesis of alkyl levulinates.

The progressive increase of greenhouse gas emission causing global warming and depletion of non-renewable fossil resources has attracted significant attention for the search of alternative sources to produce fuels and chemicals.[19–21] Organic carbon-based sources of energy are found to be the fourth largest energy source in the world to generate heat and power following oil, coal, and natural gas. They has been recognized as an alternative carbon resource to produce a variety of value-added chemicals, functional materials and fuel products due to their abundance in nature. The utilization of naturally abundant bio-renewable sources can overcome the demands for energy and chemicals without affecting food supplies.[6,22–28]

Alkyl levulinates derived from hemicellulose platforms are versatile building blocks to synthesize various chemicals and drugs owing to the presence of two functional groups, a ketone and an ester.[29] They are widely used in the food industry, as green solvents and plasticizing agents.[30,31] Moreover, they also exhibit characteristics that make them appropriate for use as cold-flow improvers in biodiesel, and as oxygenate additives for gasoline and diesel fuels owing to their low toxicity (reduced sulfur content), high lubricity, flash point stability and moderate flow properties under low temperature conditions.[32,33] Besides the applications of alkyl levulinates described above, they also serve as a precursor to synthesize γ-valerolactone (GVL), a cyclic ester that finds applications in perfumes and food industries, and as a solvent and fuel additive.[30,34–36]

Alkyl levulinates can be produced through different routes *viz.* esterification of levulinic acid and alcoholysis of furfuryl alcohol.[33] Furfuryl alcohol is recognized as an alternative feedstock to produce alkyl levulinates through alcoholysis with alkyl alcohols in the presence of acid catalysts (Scheme 1). Almost 65% of furfural (300k tons) produced worldwide is utilized to be converted into furfuryl alcohol (200k tons).[37] Thereby, the utilization of furfuryl alcohol as a precursor for one pot synthesis of alkyl levulinates *via* the alcoholysis process will be interesting. Nonetheless, furfuryl alcohol readily polymerizes to form oligomeric products in the presence of strong acids/strong acidic sites resulting in lower selectivity to alkyl levulinates. Therefore, alcoholysis of furfuryl alcohol is always carried out in a moderate yield using a large excess of alcohols to inhibit polymerization.[38] Hence, significant efforts have been recently devoted to develop catalysts for the selective synthesis of alkyl levulinates from furfuryl alcohol. Also, this reaction is challenging, and requires a catalyst which converts furfuryl alcohol into 2-(alkoxymethyl)furan (an ether) by reacting with an alkyl alcohol and subsequently converts this cyclic ether into an alkyl levulinate (keto-ester). The formation of an ester from a carboxylic acid and an alcohol is easier than that from ethers. A few metal phosphates are reported as catalysts for the synthesis of alkyl levulinates from different biomass derived chemicals namely furfuryl alcohol, cellulose and furfural.[39–41]

Herein, for the first time, an attempt is made to tailor and understand the structural properties of SnPOs synthesized by employing different SDAs which are utilized in an important challenging one-pot reaction, namely alcoholysis of furfuryl alcohol, to synthesize alkyl levulinates. The employed synthesis strategies remarkably influenced the physico-chemical properties such as surface area, morphology, and the nature and strength of acidic sites as compared to SDA-free synthesis. The catalytic behavior of SnPOs was compared with that of microporous and mesoporous aluminosilicates, and Amberlyst-15, and it surpassed the activity of conventional solid acid catalysts.

Results and discussion

Characterization of catalysts

The low angle XRD pattern of SnPO-P123 shows the absence of diffraction peaks suggesting the absence of long-range order in the pore structure of tin phosphate and is shown in ESI† Fig. S1. The wide angle XRD pattern of SnO₂-P123 (Fig. 1) shows diffraction peaks which can be indexed to the (110), (101), (200) and (211) reflections assigned to a tetragonal rutile crystal structure with the space group $P42/mnm$.[42] The wide angle XRD analysis of tin phosphates showed interesting information with the type of SDA employed during the synthesis; particularly, the crystallinity of the tin phosphate was altered with different SDAs which is depicted in Fig. 1. Notably, the wide angle XRD pattern of SnPO-P123 showed no distinct characteristic peak which suggests that the material is amorphous. However, the SnPOs synthesized using other SDAs were crystalline in nature. The observed XRD patterns are in good agreement with those of SnP₂O₇, Sn₂.₅(PO₄)₃ and SnO₂ corresponding to a cubic phase with the $Pa\bar{3}$ space group (ICDD PDF card # 00-029-1352), a rhombohedral phase with the $R\bar{3}$ space group (ICDD PDF card # 00-059-0100) and a tetragonal phase with the $P42/mnm$ space group (ICDD PDF card # 00-041-1445) respectively.
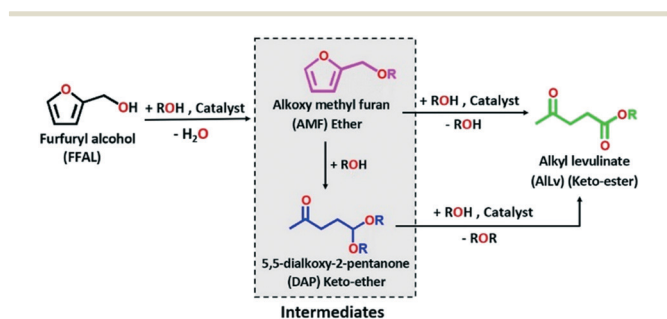
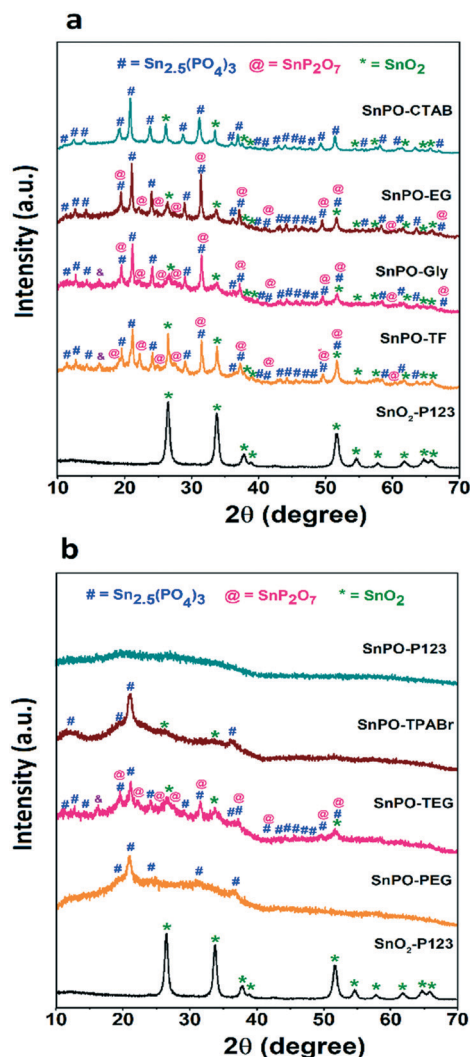**Scheme 1** Reaction scheme for alcoholysis of FFAL with alkyl alcohols.

Fig. 1 Wide angle XRD patterns of SnO₂ and SnPOs.

Fig. 2 (a) Nitrogen sorption isotherms and (b) pore size distributions of the tin phosphates; (c) FTIR spectra of (i) SnO₂–P123, (ii) as-synthesized SnPO-P123 and (iii) SnPO-P123.

The SnPOs obtained from TF, EG, GLY and TEG showed diffraction patterns well-matching with those of SnP_2O_7, $Sn_{2.5}(PO_4)_3$ and SnO_2 confirming the formation of a composite material. The other SnPOs using CTAB and TPABr showed diffraction patterns corresponding to those of $Sn_{2.5}(PO_4)_3$ and SnO_2, whereas SnPO-PEG exhibited peaks corresponding only to $Sn_{2.5}(PO_4)_3$. Broadened peaks were observed for TPABr and PEG compared with the others suggesting the formation of smaller crystallites. These results clearly suggest that the crystallization of the catalysts could be strongly influenced by the type of SDA employed during the synthesis under similar reaction conditions due to the change in chemical and physical properties associated with the SDA molecules.

The properties obtained from N_2 sorption measurements of template assisted and template free tin phosphate (SnPO) catalysts are shown in Fig. 2a and b and ESI† Fig. S2 and S3, and tabulated in Table 1. The properties like surface area, pore size and pore volume changed significantly by varying the SDA. Pluronic P123 assisted SnPO (hereafter SnPO-P123) showed a type IV isotherm with H1 type hysteresis (Fig. 2a), suggesting
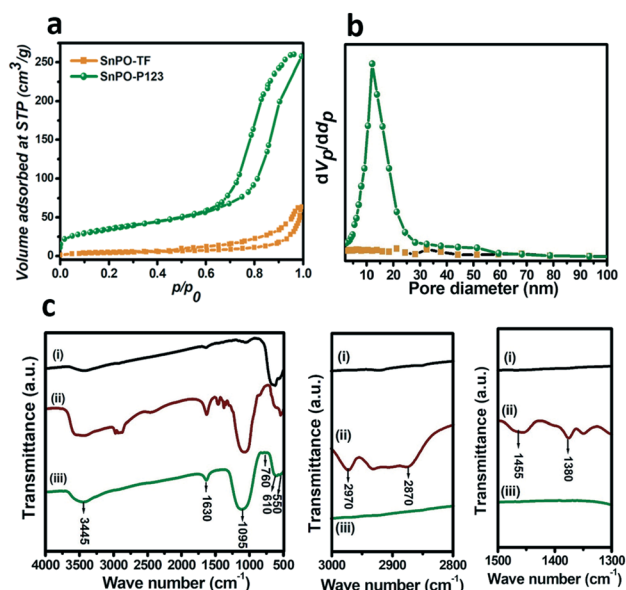
the characteristics of mesoporous materials with well-defined cylindrical like pore channels present in the porous system.[4] The BJH pore size distribution of SnPO-P123 (Fig. 2b) showed a narrow pore size of 12.1 nm confirming the presence of mesopores in the material, whereas SnPO-TF showed a multi-pore size distribution ranging from 2.5–80 nm which indicates disordered pores in the material. SnPO-P123 exhibited a significantly greater surface area (149 m² g⁻¹) and pore volume (0.5 cm³ g⁻¹) compared to the other tin phosphate catalysts. It is observed that SnPO-P123 showed an 8 times greater surface area than SnPO-TF implying the importance of the SDA for this catalyst synthesis. Therefore, it is inferred that the structural properties of SnPO can be significantly improved by providing a suitable SDA during the synthesis. The surface area of SnPO-P123 was compared with those of other catalysts adopted in this study. SnPO-P123 showed a lower surface area compared to microporous and mesoporous aluminosilicates but higher in comparison with Amberlyst-15 catalysts.

The nitrogen sorption curves of other SnPOs (ESI† Fig. S2) namely SnPO-TPABr, SnPO-CTAB, SnPO-TEG, SnPO-EG, SnPO-PEG and SnPO-GLY were type II isotherms with an H3 type hysteresis loop implying the presence of slit-shaped pores arising from non-rigid aggregates of plate-like particles. The presence of macropores (>50 nm pore size) is evident in the isotherm in view of a lack of plateau at the end of P/P_0 (near 1). From BJH pore size distribution analysis (ESI† Fig. S3), it is observed that these materials possess a multipore system ranging from 2 to 160 nm. Two SnPOs, SnPO-PEG and SnPO-GLY, exhibit a multi-pore size distribution between 2 and 30 nm, whereas others possess hierarchical meso- and macropores with a relatively wider pore size distribution at the macropore region.

The FTIR spectra of SnO₂-P123 and SnPO-P123 are depicted in Fig. 2c. The spectrum of as-synthesized SnPO-P123 showed

Table 1 Physico-chemical properties of the tin phosphates and other conventional catalysts

| Catalyst | Nitrogen sorption measurements | | | | Acidity[f] (μmol g^{-1}) | | | | | |
	Surface area[a] (m^2 g^{-1})	Pore volume[b] (cm^3 g^{-1})	Pore size[c] (nm)	B/L ratio[e]	Weak (W)	Moderate (M)	Strong (S)	Total	W + M	(W + M)/S
SnO$_2$-P123	14	0.10	37.8	0.25	15	16	9	40	31	3.4
SnPO-TF	18	0.09	21.2	1.10	68	39	13	120	107	8.2
SnPO-GLY	42	0.08	8.1	1.33	70	54	16	140	124	7.8
SnPO-EG	39	0.14	13.8	1.38	75	84	21	180	159	7.6
SnPO-CTAB	53	0.24	13.8	1.46	84	92	24	200	176	7.3
SnPO-PEG	75	0.19	7.1	1.50	100	98	32	230	198	6.2
SnPO-TEG	64	0.27	7.1	1.55	160	200	60	420	360	6.0
SnPO-TPABr	97	0.44	7.1	1.88	218	210	72	500	428	5.9
SnPO-P123	149	0.50	12.1[d]	1.92	232	230	88	550	462	5.3
H-Beta	485	0.44	[h]	1.40	212	396	142	750	608	4.3
Al-MCM-41	947	0.76	3.5[d]	1.72	254	142	154	550	396	2.6
Amberlyst-15	39	0.16	23.3	∞	—	—	—	4700[g]	—	—

[a] BET surface area. [b] Total pore volume. [c] Mean pore diameter. [d] From BJH pore size analysis. [e] Py-FTIR. [f] NH$_3$-TPD. [g] Acid–base titration. [h] 0.66 × 0.67 and 0.56 × 0.56.

bands in the region ~2870 and ~2960 cm^{-1} corresponding to C–H stretching vibrations of the SDA. The bands at 1380 and 1455 cm^{-1} correspond to C–C vibrations and C–H bending vibrations of methylene groups of the SDA. These bands are absent in the calcined SnPO-P123 suggesting the complete removal of P123 after calcination. The FTIR spectrum of SnPO-P123 showed a broad band from 850 to 1350 cm^{-1} (centered at around 1095 cm^{-1}), which was absent in SnO$_2$-P123. It corresponds to asymmetric Sn–O–P stretching vibration and indicates the presence of a phosphate framework in the SnPO.[4] The spectra of SnO$_2$-P123 and SnPO-P123 showed a broad band centered at 3445 cm^{-1} and a weak band at 1630 cm^{-1} ascribed to the stretching and bending vibrations of hydroxyl groups (–OH) of adsorbed water molecules, respectively. Moreover, SnO$_2$-P123 showed peaks at 630 and 535 cm^{-1} which are attributed to Sn–O stretching vibration. The spectrum of SnPO-P123 showed a weak band at ~760 cm^{-1} due to the asymmetric vibration of bridging P–O–P bonds, and the other two bands at 615 and 550 cm^{-1} correspond to the bending vibration of PO$_2$.[17]

The nature of acidic sites in SnO$_2$, SnPO and other catalysts were investigated by the pyridine-FTIR technique and the spectra are depicted in Fig. 3a and b and ESI† Fig. S4. The interaction of pyridine with the Brønsted (denoted as B) and Lewis acid sites (denoted as L) gives rise to bending vibrations at 1540 and 1450 cm^{-1} respectively.[27] The band at around 1490 cm^{-1} is ascribed to the overlapping of Brønsted and Lewis acid sites. The acidic sites in SnO$_2$-P123 determined by pyridine-FTIR, showed a higher amount of Lewis acidic sites with a B/L ratio of 0.25, i.e. 75% of acidic sites are of Lewis character which is depicted in ESI† Fig. S4. The SnPO catalysts exhibited a combination of Brønsted and Lewis acidic sites; the presence of Brønsted acidity in the catalysts could be attributed to surface –OH groups (P–OH), whereas the Lewis acidity is ascribed to tin in a tetrahedral coordination within the Sn–O–P framework and coordinatively unsaturated tin ions.[17] The relative ratio of Brønsted to Lewis acidity in SnPO varied with the use of

different SDAs. Moreover, SnPO-TF also exhibited both types of acidic sites as observed with SDA assisted tin phosphates. Among the tin phosphates, SnPO-P123 and SnPO-TPABr showed a greater B/L ratio of 1.9. The B/L ratio of SnPO-SDA decreased in the order SnPO-P123 ≈ TPABr > TEG > PEG > CTAB ≈ EG > glycerol. Thus, these results confirm that the acidic sites in tin phosphate can be tuned by employing different structure directing agents as a modulator. The py-FTIR of other catalysts namely H-beta and Al-MCM-41 showed a decrease in the B/L ratio compared to that of SnPO-P123 (shown in Fig. S4†).

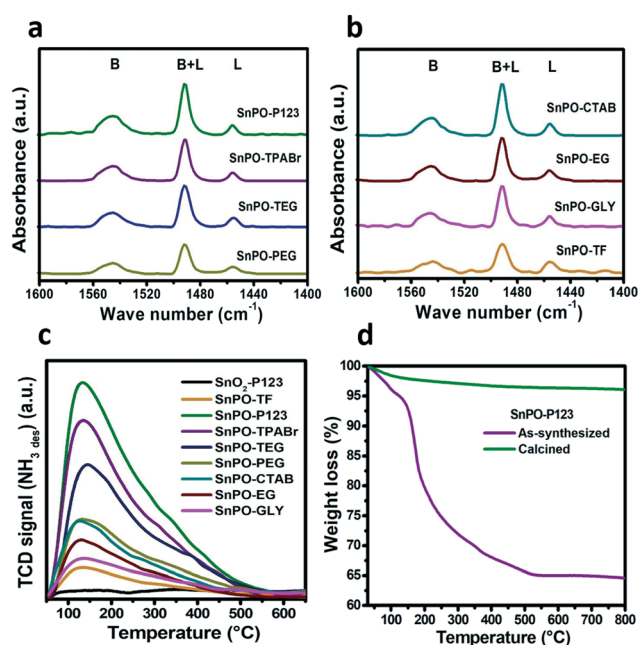The amount of acidic sites in SnPO and other catalysts was determined by the NH$_3$-TPD technique as shown in

Fig. 3 Acidity measurement: (a and b) pyridine-FTIR profiles of tin phosphates, (c) NH$_3$-TPD profiles of tin oxide and tin phosphates, and (d) thermogravimetric analysis profiles of SnPO-P123.
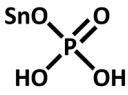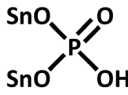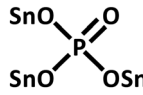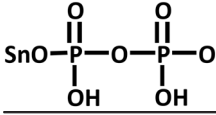
Table 1. The TPD profiles of the SnPO catalysts are presented in Fig. 3c. The tin phosphates synthesized using different SDAs exhibited a difference in the total number of acidic sites. SnPO-P123 contained 550 µmol g^{-1} of total acidity which is greater than those of the other tin phosphate catalysts studied in this work. The tin oxide (SnO$_2$-P123) catalyst exhibited a low acidity of 40 µmol g^{-1} which signifies the key role of the phosphate source in generating acidic sites. SnPO-P123 showed 4.5 times higher acidity compared to SnPO-TF which could be due to its larger surface area leading to a greater availability of surface active sites. The total acidity in the tin phosphates prepared using different SDAs decreases in the order P123 > TPABr > TEG > PEG > CTAB > EG > GLY. The acidic strengths of the catalysts are quantified by deconvolution of the peaks obtained from NH$_3$-TPD and are listed in Table 1. The strength of acidic sites is distinguished as weak (50–150 °C), moderate (150–350 °C) and strong (>350 °C) based on desorption temperatures. The weak and moderate acidic sites of SnPO increase with the increase in total acidity. Interestingly, the sum of weak and moderate ($W + M$) acidic sites of the SnPO catalysts was 5 to 8 times greater as compared with the strong acidic sites. Notably, the Sn and P content in different tin phosphates varied relatively with respect to the different SDAs as shown in Table S1.† The difference in the concentrations of the main constituents of tin phosphate synthesized with different SDAs can be related to the diversity in their chemical and structural properties. However, the conventional solid acid catalysts like microporous and mesoporous aluminosilicates, showed a lower ($W + M$)/S ratio ranging from 2 to 4 confirming the presence of stronger acidic sites compared to the SnPO catalysts which is depicted in ESI† Fig. S5.

The thermogravimetric analysis (TGA) profiles of as-synthesized and calcined SnPO-P123 are shown in Fig. 3d. As-synthesized SnPO-P123 showed a weight loss in two regions; the initial weight loss of 6% below 120 °C is attributed to the loss of water molecules. The second weight loss in the region of 120–530 °C is ascribed to the removal of SDA. No weight loss was observed above 530 °C suggesting the complete removal of SDA at around 530 °C. The calcined SnPO-P123 showed a negligible weight loss as compared to the as-synthesized material indicating the complete removal of SDA.

The selected SnPO samples were characterized by the ^{31}P MAS NMR technique to identify the nature and distribution of phosphorus environments in the bulk phase formed due to the employment of different SDAs during the synthesis. The chemical shifts and relative intensities of ^{31}P MAS NMR peaks are summarized in Table 2. Generally, a transition of the chemical shift to more negative values is indicative of both an increase in the number of P–O–Sn bonds and an increase in the chain length of the phosphorus atoms. The latter corresponds to progressive deprotonation and subsequent condensation of phosphate species (P–O–P bonds) that typically occurs during calcination.[2,43–45] Fig. 4 shows the NMR spectra of the four tin phosphate samples. The resonance peak in the range of −5 to −7 ppm is attributed to tetrahedral phosphates bonded to one tin group and two hydroxyl groups (Sn–O)–PO(OH)$_2$.[46] This coordination gives way to geminal P–(OH) groups. The signal from −12 to −15 ppm signifies the presence of two tin groups and one hydroxyl group bonded to phosphate (Sn–O)$_2$–PO(OH).[47] The resonance peaks at a chemical shift of −20 to −23 ppm can be assigned to tetrahedral phosphate connected with three tin groups (Sn–O)$_3$–PO, whereas the peaks in the range of −29 to −33 ppm indicates the formation of polyphosphates or P–O–P due to condensation of phosphate species.[2]

The NMR spectra of the four samples showed different relative ratios associated with the phosphorus environment. The resonance peaks associated with SnPO-P123 were broader and different than those of SnPO-TF. SnPO-P123 possessed relatively broader peaks due to its amorphous nature. It showed two different resonance peaks at −5.7 and −12.6 ppm assigned to phosphorus with an undissociated P–OH group which is considered as a Brønsted acidic site. This confirms that the high amount of Brønsted acidic sites in these materials is due to the presence of a higher amount of surface P–OH groups. This is also evident from Py-FTIR as it showed a greater B/L ratio for the SnPO-P123 catalyst. Importantly, SnPO-TF showed a significant difference in the distribution of phosphate species compared to the other SnPOs such as SnPO-P123, SnPO-CTAB and SnPO-TPABr. Also, it can be further inferred from the relative amounts of phosphate species in the catalysts that the enhancement of P–OH species varies with the different structure directing agents and is found to be greater compared with that from

Table 2 Identification and quantification of the different phosphate species in the tin phosphate catalysts from ^{31}P MAS NMR spectroscopy

Chemical shift (ppm)	−5 to −7	−12 to −17	−20 to −23	−27 to −38
Coordination states of P	SnO–P(=O)(HO)(OH)	SnO–P(=O)(SnO)(OH)	SnO–P(=O)(SnO)(OSn)	SnO–P(=O)(OH)–O–P(=O)(OH)–O
Catalyst	Chemical shift (ppm) and relative amount (%) in parentheses			
SnPO-P123	−5.7 (25.6)	−12.6 (32.0)	−20.8 (32.6)	−31.0 (9.6)
SnPO-TF	−6.1 (7.4)	−14.7 (16.3)	−22.7 (36.7)	−28.8 & −37.9 (39.7)
SnPO-CTAB	−5.0 (20.8)	−15.1 (34.6)	−21.9 (27.2)	−27.4 (17.4)
SnPO-TPABr	−5.5 (12.2)	−12.9 (27.3)	−22.4 (41.7)	−33.3 (19.8)

Fig. 4 ^{31}P MAS NMR spectra of SnPOs.

Fig. 5 SEM images of the different SnPOs.
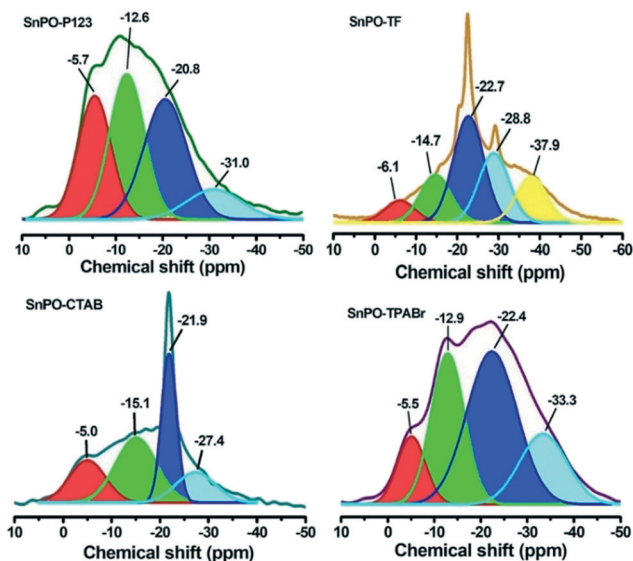
template free synthesis (SnPO-TF). Additionally, the degree of condensation of phosphate species (P–O–P) was reduced by employing a structure directing agent during the synthesis. This confirms that the structure directing agents also influence the nature and amount of phosphate species in addition to the formation of pores.

The SEM images of the SnPOs synthesized with SDAs as well as the template free method are depicted in Fig. 5 and ESI† Fig. S6. The images revealed different structures and particle sizes like spherical, flower-like, flake-like and sponge-like morphologies mostly in the nanosize range depending on the type of SDA employed during the synthesis. These results suggest that the morphological properties of the SnPOs are not the same even though they are constructed from the same Sn, P and O elements. SnPO-P123 showed nano-sized spherical particles with a size ranging between 15 and 35 nm. On the other hand, SnPO-TF showed an irregular particle size and morphology significantly different from the SDA assisted SnPOs which could be due to uncontrolled growth of particles in the absence of a SDA. Interestingly, in SnPO-TEG, the flakes are arranged to form a hierarchical structure yielding a flower-like morphology, whereas SnPO-PEG possessed flake-like particles stacked randomly leading to an irregular morphology. In SnPO-CTAB, agglomerated spherical particles were fused to form a sponge-like morphology, whereas SnPO-TPABr contained thin flakes in random orientations which are loosely held together. The SEM image of SnPO-GLY showed an irregular morphology in the nanosize range, where particles were stacked upon one another (ESI† Fig. S6). Thus, SEM analyses show that the SDA has a vital role in controlling the size and morphology of SnPO particles during synthesis. The change in structural architecture of SnPOs by employing different SDAs could be associated with the formation of micelles in different orientations leading to
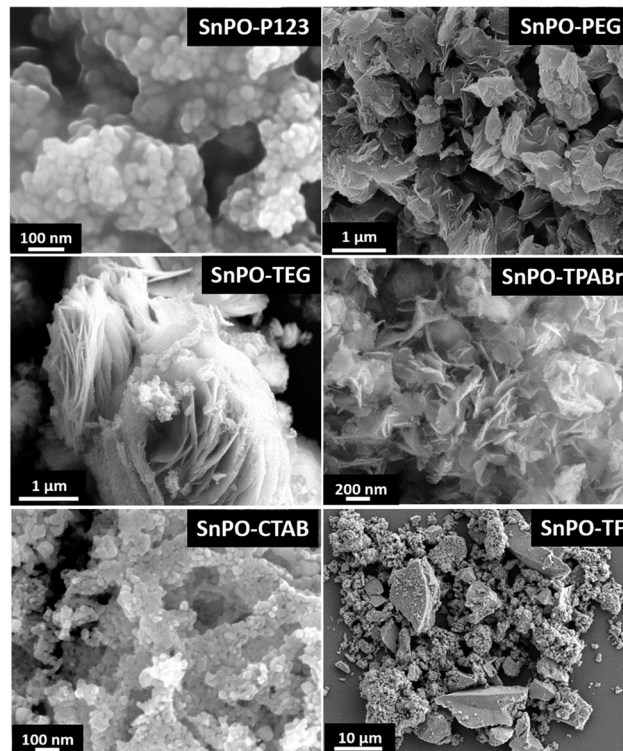
varied self-assembly resulting in the growth of SnPOs with different morphologies. It is clear that, by using an appropriate synthesis strategy, it is possible to tune and control explicitly both the catalyst morphology and the nature of active sites at the same time as evidenced by the structural and chemical analysis in this work.

The TEM images of SnPO-P123 with bright field and SAED patterns are depicted in ESI† Fig. S7. The bright field images (ESI† Fig. S7 a–e) showed a wormhole-like topology and the presence of mesopores with a pore size ranging between 5 and 15 nm, which is well in agreement with the BJH pore size distribution through nitrogen sorption analysis. This also confirms the presence of mesopores in SnPO-P123 which could be attributed to the voids formed between the clusters of particles formed by interactions of tin phosphate nanoparticles. The TEM image shows that SnPO-P123 possesses a spheroidal morphology with nanosized particles ranging from 8–16 nm with an average particle size of 12 nm. The SAED pattern (ESI† Fig. S7f) of SnPO-P123 showed diffused rings without a diffraction spot implying that the material is amorphous in nature which is in agreement with XRD analysis.

Catalytic activity studies

Alcoholysis of furfuryl alcohol with alkyl alcohols. Various acid catalysts have been reported for alcoholysis of furfuryl alcohol, *viz.* mineral acids and metal salts (homogeneous),[48,49] zeolites, acid resins,[50,51] metal organic

frameworks,[52] mesoporous materials (Al-TUD-1, Al-SBA-15),[53–55] ionic liquids,[56] organic–inorganic hybrid acid catalysts,[57] supported heteropolyacids,[58,59] acidic carbon–silica composite materials,[60] activated carbon (microwave assisted reaction),[61] sulfated zirconia[62] and sulfonic acid functionalized materials.[38] From these reports, it is well understood that the Brønsted acid sites play a vital role in the selective synthesis of alkyl levulinates. Neves *et al.* reported a significant decline in ethyl levulinate yield from 90 to 74% in the third run during the catalyst reusability study of Amberlyst-15 (ref. 53). Zhang *et al.* reported a drastic decrease in *n*-butyl levulinate yield from 83 to 65% during the second run of an organic–inorganic hybrid solid acid catalyst ([BmimSO$_3$H]$_3$PW$_{12}$O$_{40}$).[57] The authors claimed that the severe catalyst deactivation is due to the accumulation of oligomeric products formed by furfuryl alcohol polymerization during the reaction which preferably adsorbed on active sites of the solid acid catalyst and are difficult to remove by simple solvent extraction. The solid acid catalyst can be effectively regenerated by burning-off the organic deposits at high temperatures, but it is not possible for a catalyst possessing a low thermal stability. Also, under most of the reaction conditions, alkyl alcohols are used in large excess to inhibit furfuryl alcohol polymerization. Hence, this has driven us to design a catalyst possessing high thermal stability with acidic sites of moderate strength and a greater amount of Brønsted acid sites to suppress the rapid polymerization of furfuryl alcohol during reaction, thereby the use of excess alkyl alcohols could be minimized.

Catalytic behavior of the tin phosphates and other catalysts for alcoholysis of furfuryl alcohol with *n*-butanol

The catalytic performance of the tin phosphates was studied for alcoholysis of furfuryl alcohol with 1-butanol and the results are presented in Table 3. The influence of time on the progress of reaction using the tin phosphates and tin oxide are shown in ESI† Fig. S8. A blank run without a catalyst showed only 0.1% furfuryl alcohol conversion indicating that the reaction is truly catalytic. The catalytic activity of the template assisted tin phosphates (SnPO-SDA) was compared with that of the template free tin phosphate (SnPO-TF). The SnPO-TF catalyst gave 47.6% furfuryl alcohol conversion with 8.4% BuLv yield which is much lower compared to that with the template assisted tin phosphate catalysts. The lower catalytic performance of SnPO-TF could be attributed to the presence of a lower amount of acidic sites, less surface area and disordered pores in the catalyst. The tin phosphates (SnPOs) synthesized with various structure directing agents showed a difference in their catalytic performance due to the change in their structural and chemical properties as observed from nitrogen sorption, XRD and acidity measurements. The SnPO-SDA catalysts showed an increase in furfuryl alcohol conversion from 51.4 to 100% and an increase in BuLv yield from 12.3 to 28.6% for a 2 h reaction because of the increase in total weak and moderate acidic sites (124 to 462 µmol g^{-1}) and B/L ratio (1.3 to 1.9). Among the catalysts, SnPO-P123 exhibited superior activity to those of the other catalysts by showing complete furfuryl alcohol conversion in 2 h with a greater yield of BuLv (28.6%). The SnPO-SDA catalysts showed a decrease in BuLv yield in the order SnPO-P123 > -TPABr > -TEG > -PEG > -CTAB > -EG > -GLY. The tin oxide (SnO$_2$-P123) catalyst, on the other hand, gave lowest activity with only 4% furfuryl alcohol conversion and 0.2% BuLv yield (6% BuLv selectivity). The poor catalytic performance of tin oxide could be due to the presence of a low number of acidic sites (31 µmol g^{-1}) in the catalyst.

The multi-step transformation of furfuryl alcohol to BuLv is challenging and requires a catalyst which possesses acidic sites, predominantly of Brønsted acidity. To understand the

Table 3 Catalytic activity of the tin phosphates for alcoholysis of furfuryl alcohol with 1-butanol

Catalyst	B/L ratio	$W + M$ acidity (µmol g^{-1})	FFAL conv. (mol%)	Product selectivity (mol%)				BuLv yield (mol%)
				BMF	DBP	BuLv	Others	
Blank[a]	—	—	0.1	100.0	0.0	0.0	0.0	0.0
SnO$_2$-P123	0.25	31	3.9	80.9	0.8	6.4	11.9	0.2
SnPO-TF	1.10	107	47.6	61.0	5.6	17.6	15.7	8.4
SnPO-GLY	1.33	124	51.4	57.7	4.9	24.0	13.3	12.3
SnPO-EG	1.38	159	68.6	59.7	7.2	25.5	7.7	17.5
SnPO-CTAB	1.46	176	74.9	54.5	6.0	25.8	13.7	19.3
SnPO-PEG	1.50	198	80.2	59.0	6.0	26.4	8.6	21.2
SnPO-TEG	1.55	360	86.1	58.4	5.9	26.6	9.1	22.9
SnPO-TPABr	1.88	428	92.9	57.7	6.6	27.1	8.6	25.2
SnPO-P123	**1.92**	**462**	**100.0**	**58.2**	**5.6**	**28.6**	**7.6**	**28.6**

Reaction conditions: furfuryl alcohol (FFAL) (0.4 g, 4 mmol), 1-butanol (3.1 g, 40 mmol), catalyst = 0.1 g (0.025 g$_{cat}$ mmol$_{FFAL}$$^{-1}$), reaction temperature = 120 °C, time = 2 h. [a] Time = 6 h, BMF = 2-(butoxymethyl)furan, BuLv = butyl levulinate, DBP = 5,5-dibutoxy-2-pentanone, mass balance for all reactions >98%.

correlation of catalytic activity with active sites, graphs of the amount of weak + moderate acidic sites and B/L ratio *vs.* BuLv yield are plotted (Fig. 6). The trend shows an increase in BuLv yield with an increase in both acidity and B/L ratio in tin phosphate suggesting the significance of the amount and nature of acidic sites towards the reaction. Interestingly, SnPO-TPABr containing a comparably similar amount of acidic sites with respect to SnPO-P123 showed a lower catalytic activity. The lower performance of the former could be due to the lower surface area and disordered pores in the catalyst compared to those in SnPO-P123. Therefore, it is evident from the study that the superior performance of SnPO-P123 to that of the other tin phosphates is attributed to the synergistic effect of the amount and nature of acidic sites, mesoporosity and enhanced surface area, resulting in a better distribution of active sites in catalysts. This provides easy accessibility to the substrates and facilitates easy diffusivity of molecules. Thus, the SnPO-P123 catalyst was selected as the best catalyst for further studies. Also, the catalytic performance of the active catalyst SnPO-P123 was evaluated with other well-known conventional microporous and mesoporous catalysts, namely H-beta, Al-MCM-41 and Amberlyst-15. Among them, SnPO-P123 outperformed the other catalysts by exhibiting higher BuLv yield with a TON for BuLv production of 17 as shown in Table S2.†

Determination of active sites in SnPO-P123 for alcoholysis

To clarify the nature of active sites in SnPO-P123 responsible for alcoholysis of furfuryl alcohol, the reaction was carried out with the catalyst which was pretreated with basic 2,6-lutidine and the experimental details are given in ESI† S1.2.4. It is known that 2,6-lutidine selectively interacts with Brønsted acid sites but not with Lewis acid sites due to steric h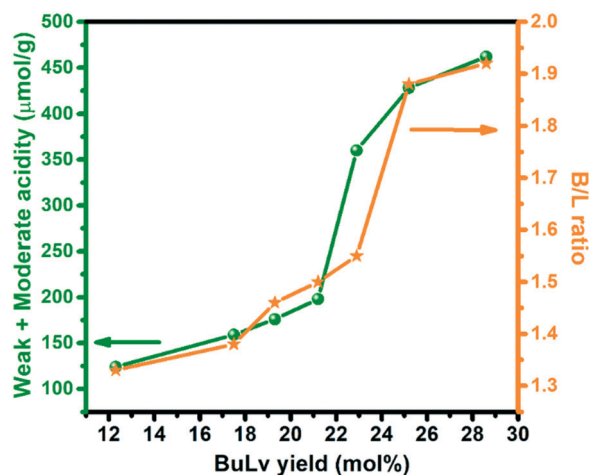indrance caused by its methyl groups.[63,64] Therefore, this results in exposure and participation of only Lewis acidic Sn^{4+} sites during the reaction. Thus, for the 2,6-lutidine-treated SnPO-P123 catalyst, only 16% furfuryl alcohol conversion at 90 min was obtained which means that the activity was suppressed by blocking the Brønsted acidic sites (Fig. 7a). The untreated SnPO-P123 gave 100% furfuryl alcohol conversion which is significantly higher compared to that for the 2,6-lutidine treated SnPO-P123 catalyst. Fig. 7b shows that the contribution of Lewis acidic Sn sites towards the alcoholyis reaction is negligible (16%) compared with that of Brønsted acid sites (84%). Therefore, this confirms that the Brønsted acid sites in the SnPO-P123 catalyst govern as the active sites for the alcoholysis reaction.

The reaction conditions play an important role in obtaining higher product yields and influence the catalyst performance. Thus, the alcoholysis of furfuryl alcohol was studied using different reactant mole ratios, catalyst amounts and reaction temperatures, and a detailed explanation is given in the ESI† (Fig. S9 and S10). Under the optimized reaction conditions of catalyst concentration, 0.1 g_{cat} $mmol_{FFAL}^{-1}$; FFAL: 1-butanol mole ratio of 1:10 and 160 °C, 100% conversion and 94% BuLv selectivity are achieved in 3 h reaction time.

Influence of substrates on the synthesis of alkyl levulinates

The potential application of SnPO-P123 was further assessed to synthesize a variety of alkyl levulinates by carrying out
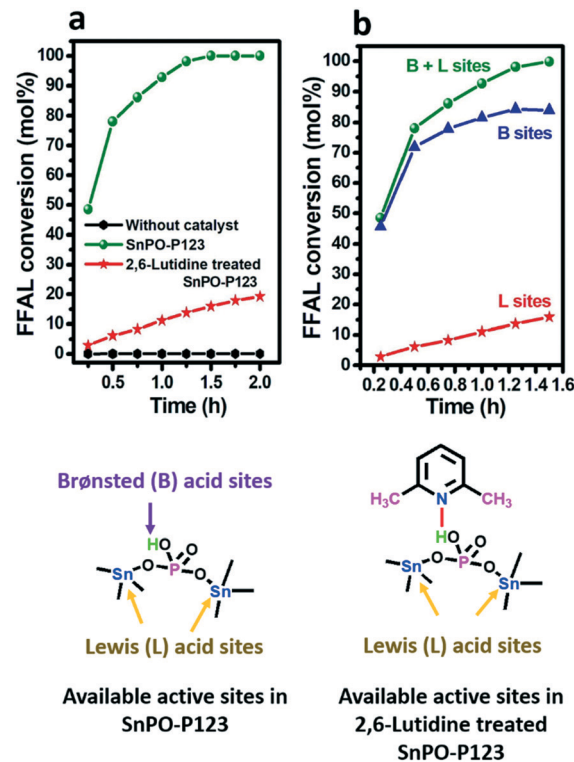

Fig. 6 Correlation plots of butyl levulinate yield *vs.* the total amount of acidic sites (mmol NH_{3des} g^{-1}) and B/L ratio. Reaction conditions: furfuryl alcohol (FFAL) (0.4 g, 4 mmol), 1-butanol (3.1 g, 40 mmol), catalyst = 0.1 g (0.025 g_{cat} $mmol_{FFAL}^{-1}$), reaction temperature = 120 °C, time = 2 h, BuLv = butyl levulinate.

Fig. 7 (a) Catalytic performance of 2,6-lutidine treated and untreated SnPO-P123 catalysts for alcoholysis of furfuryl alcohol. (b) Contribution of different active sites responsible for the alcoholysis reaction. The L site value is the difference between the B + L site and B site values.

alcoholysis of furfuryl alcohol with different alkyl alcohols to explore the substrate scope and the results are tabulated in Table 4. The reaction was carried out at 140 °C with a FFAL-to-alcohol molar ratio of $1:10$ at 0.1 g_{cat} $mmol_{FFAL}^{-1}$ for 3 h. 100% furfuryl alcohol conversion was achieved for the alcohols studied in this work, but the alkyl levulinate selectivity (or yield) achieved ranged from 77.5 to 91.8%. The alkyl levulinate selectivity was compared at 2 h reaction time to study the difference in activities. A decrease in alkyl levulinate selectivity from 89.9 to 68.4% was observed with an increase in alcohol chain length from methanol (C_1) to n-butanol (C_4). The decrease in activity with the increase of alkyl chain length could be associated with a decrease of the dielectric constant[60] for different alcohols and also the difficulty in the conversion of the formed intermediate 2-(alkoxymethyl)furan (major) into alkyl levulinates is ascribed to a longer carbon chain length.[48,56] Interestingly, butanolysis of furfuryl alcohol at 160 °C for 3 h gave 94.6% BuLv yield suggesting that temperature plays a vital role in converting BMF to BuLv.

Leaching and catalyst reusability studies

A leaching test of SnPO-P123 was carried out to investigate the leaching of active sites in the catalyst during reaction. For the alcoholysis reaction, BMF is an intermediate which converts into the final product gradually in the presence of a catalyst even after furfuryl alcohol is completely converted in the initial phase of the reaction itself. Hence, a leaching study is important to understand if leached species catalyze the intermediate into the final product. For the leaching test, the reaction was stopped at 15 min achieving 51% BMF and 39.6% BuLv selectivity where 100% furfuryl alcohol was converted, and the reaction mixture containing the catalyst was removed by centrifugation (ESI† Fig. S12a). Later, the filtrate was allowed to undergo reaction without a catalyst which showed no further improvement in BuLv selectivity confirming that the catalyst is truly heterogeneous.

Table 4 Impact of substrate on the yield of alkyl levulinates using SnPO-P123

Sl. No.	Substrate	Dielectric constant[a]	Time (h)	Temp (°C)	Yield (mol%)	
					AMF	AlLv
1	MeOH	33.0	2	140	0.0	89.9
2	MeOH	33.0	3	140	0.0	91.8
3	EtOH	25.3	2	140	1.5	85.6
4	EtOH	25.3	3	140	0.0	90.1
5	1-PrOH	20.8	2	140	4.2	80.4
6	1-PrOH	20.8	3	140	2.0	88.4
7	1-BuOH	17.8	2	140	24.3	68.4
8	1-BuOH	17.8	3	140	13.4	77.5
9	1-BuOH	17.8	2	160	10.2	82.8
10	1-BuOH	17.8	3	160	1.1	94.6

Reaction conditions: furfuryl alcohol (FFAL) (1.6 g, 16 mmol), alcohol (160 mmol), catalyst = 0.10 g_{cat} $mmol_{FFAL}^{-1}$, AMF = 2-(alkoxymethyl) furan, AlLv = alkyl levulinate. Conversion of FFAL = 100%. [a] DC = dielectric constant from ref. 65, mass balance for all reactions >95%.

The reusability of the SnPO-P123 catalyst was examined under optimized reaction conditions for four consecutive runs (fresh, R-1, R-2 and R-3). For the butanolysis reaction, it maintains a BuLv selectivity >93% with 100% furfuryl alcohol conversion (ESI† Fig. S12b). These results suggest that the SnPO-P123 catalyst is stable and reusable without any considerable loss in activity and proves to be a potential catalyst for alcoholysis reactions to produce alkyl levulinates in high yields. Importantly, SnPO-P123 was found to be an excellent catalyst compared to the reported catalysts in the literature to yield alkyl levulinates at a shorter reaction time (3 h) with a lower reactant mole ratio ($1:10$) confirming its potential in catalysis (ESI† Table S3).

Study of the spent catalyst

The spent SnPO-P123 catalyst after 4 runs was characterized by the FTIR, nitrogen sorption and NH$_3$-TPD techniques. The FTIR analysis of the used catalyst shows no changes in the spectrum compared with that of the fresh catalyst confirming that the spent catalyst retains its functional groups (ESI† Fig. S13). The XRD pattern of recycled SnPO-P123 was similar to that of the fresh catalyst, suggesting no structural changes after the reaction (ESI† Fig. S14). The nitrogen sorption analysis of the spent catalyst showed a similar surface area, pore size and pore volume compared to those of the fresh catalyst showing that the catalyst retains its surface properties even after 4 cycles (ESI† Table S4). Also, NH$_3$-TPD measurements showed a marginal decrease in the amount of acidic sites (by 20 μmol g^{-1}) compared to that in the fresh catalyst (ESI† Table S4). Thus, the physico-chemical properties of the spent catalyst prove that the catalyst is stable under the reaction conditions.

Conclusions

We performed a comprehensive assessment on tin phosphate synthesis for one-pot synthesis of alkyl levulinates from furfuryl alcohol and revealed stark differences in the reactivity as a function of variable properties caused by structure directing agents (SDAs) employed during the synthesis. Employing SDAs greatly influenced the structural and chemical properties of the SnPOs. Importantly, ^{31}P MAS NMR proves the presence of different types of phosphorous species and that the relative concentration of P–OH sites in the catalyst is associated with the SDA adopted in synthesis. XRD studies reveal the formation of tin phosphate with variable crystal structures (cubic and rhombohedral) and suggest that the crystallization of catalysts is strongly influenced by the type of SDA associated with the change in the chemical and physical properties. Among the SnPOs, SnPO-P123 exhibited a greater surface area, a higher number of acidic sites and mesoporosity with a narrow pore size distribution. Interestingly, the flexibility in tuning and control of morphology, particle size, and acidic sites with different amounts, nature and strength directed by SDA is noteworthy. Also, the active centers responsible in the SnPO

catalysts for the alcoholysis reaction are elucidated by probing with 2,6-lutidine which confirms the importance of Brønsted acidic sites.

SnPOs directed by different SDAs exhibited different reactivities towards the synthesis of butyl levulinate. In particular, the SnPO-P123 catalyst showed high catalytic activity in butanolysis of furfuryl alcohol with 94.6% selectivity to butyl levulinate and 100% FFAL conversion, thus rivalling the best catalyst reported to date at a lower molar ratio of furfuryl alcohol to butyl alcohol. A good correlation of the catalytic activity of the SnPOs with the total weak and moderate acid sites and B/L ratio was obtained for the butanolysis reaction. The alcoholysis of furfuryl alcohol with C_1–C_4 alcohols gave invariably high yields (>88%) for different alkyl levulinates. Importantly, the SnPO-P123 catalyst showed exceptional reactivity compared to conventional solid acid catalysts. This could be attributed to the unique combination of chemical and structural properties of the catalyst and proves its potential catalytic behavior. Overall, this synthetic approach and characterization represents new opportunities to tailor the physico-chemical properties of tin phosphate for a wide range of catalytic applications.

Conflicts of interest

The authors declare no competing financial interests.

Acknowledgements

References

1 U. R. Pillai and E. Sahle-Demessie, *Chem. Commun.*, 2004, 826–827.

2 R. Weingarten, Y. T. Kim, G. A. Tompsett, A. Fernández, K. S. Han, E. W. Hagaman, W. C. Conner Jr, J. A. Dumesic and G. W. Huber, *J. Catal.*, 2013, **304**, 123–134.

3 X.-Z. Lin, Z.-Z. Yang, L.-N. He and Z.-Y. Yuan, *Green Chem.*, 2015, **17**, 795–798.

4 A. Dutta, D. Gupta, A. K. Patra, B. Saha and A. Bhaumik, *ChemSusChem*, 2014, **7**, 925–933.

5 Q. Hou, M. Zhen, L. Liu, Y. Chen, F. Huang, S. Zhang, W. Li and M. Ju, *Appl. Catal., B*, 2018, **224**, 183–193.

6 P. Manjunathan, M. Kumar, S. R. Churipard, S. Sivasankaran, G. V. Shanbhag and S. P. Maradur, *RSC Adv.*, 2016, **6**, 82654–82660.

7 D. Gu and F. Schüth, *Chem. Soc. Rev.*, 2014, **43**, 313–344.

8 V. S. Marakatti, P. Manjunathan, A. B. Halgeri and G. V. Shanbhag, *Catal. Sci. Technol.*, 2016, **6**, 2268–2279.

9 T.-Y. Ma, L. Liu and Z.-Y. Yuan, *Chem. Soc. Rev.*, 2013, **42**, 3977–4003.

10 S. R. Churipard, P. Manjunathan, P. Chandra, G. V. Shanbhag, R. Ravishankar, P. V. Rao, G. S. Ganesh, A. Halgeri and S. P. Maradur, *New J. Chem.*, 2017, **41**, 5745–5751.

11 Y. Zhang, J. Wang, J. Ren, X. Liu, X. Li, Y. Xia, G. Lu and Y. Wang, *Catal. Sci. Technol.*, 2012, **2**, 2485–2491.

12 X.-Z. Lin, T.-Z. Ren and Z.-Y. Yuan, *Catal. Sci. Technol.*, 2015, **5**, 1485–1494.

13 L. Cheng, X. Guo, C. Song, G. Yu, Y. Cui, N. Xue, L. Peng, X. Guo and W. Ding, *RSC Adv.*, 2013, **3**, 23228–23235.

14 A. Jain, A. M. Shore, S. C. Jonnalagadda, K. V. Ramanujachary and A. Mugweru, *Appl. Catal., A*, 2015, **489**, 72–76.

15 H. Xu, Z. Miao, H. Zhao, J. Yang, J. Zhao, H. Song, N. Liang and L. Chou, *Fuel*, 2015, **145**, 234–240.

16 P. Półrolniczak and S. Kowalak, *J. Porous Mater.*, 2011, **18**, 703–706.

17 X. Wang, F. Liang, C. Huang, Y. Li and B. Chen, *Catal. Sci. Technol.*, 2015, **5**, 4410–4421.

18 X. Wang, F. Liang, C. Huang, Y. Li and B. Chen, *Catal. Sci. Technol.*, 2016, **6**, 6551–6560.

19 S. Dutta, S. De, B. Saha and M. I. Alam, *Catal. Sci. Technol.*, 2012, **2**, 2025–2036.

20 X. Zhang, K. Wilson and A. F. Lee, *Chem. Rev.*, 2016, **116**, 12328–12368.

21 S. Sandesh, P. K. R. Kristachar, P. Manjunathan, A. Halgeri and G. V. Shanbhag, *Appl. Catal., A*, 2016, **523**, 1–11.

22 Z. Zhang, J. Song and B. Han, *Chem. Rev.*, 2016, **117**, 6834–6880.

23 H. Li, A. Riisager, S. Saravanamurugan, A. Pandey, R. S. Sangwan, S. Yang and R. Luque, *ACS Catal.*, 2017, **8**, 148–187.

24 P. P. Upare, A. Chamas, J. H. Lee, J. C. Kim, S. K. Kwak, Y. K. Hwang and D. W. Hwang, *ACS Catalysis*, 2019.

25 P. Manjunathan, R. Ravishankar and G. V. Shanbhag, *ChemCatChem*, 2016, **8**, 631–639.

26 A. H. Valekar, M. Lee, J. W. Yoon, J. Kwak, D.-Y. Hong, K.-R. Oh, G.-Y. Cha, Y.-U. Kwon, J. Jung and J.-S. Chang, *ACS Catal.*, 2020, **10**, 3720–3732.

27 P. Manjunathan, S. P. Maradur, A. Halgeri and G. V. Shanbhag, *J. Mol. Catal. A: Chem.*, 2015, **396**, 47–54.

28 S. Sandesh, P. Manjunathan, A. B. Halgeri and G. V. Shanbhag, *RSC Adv.*, 2015, **5**, 104354–104362.

29 Z. Zhang, K. Dong and Z. K. Zhao, *ChemSusChem*, 2011, **4**, 112–118.

30 A. Démolis, N. Essayem and F. Rataboul, *ACS Sustainable Chem. Eng.*, 2014, **2**, 1338–1352.

31 R. Marcel, T. Durillon, L. Djakovitch, F. Fache and F. Rataboul, *ChemistrySelect*, 2019, **4**, 3329–3333.

32 M. J. Climent, A. Corma and S. Iborra, *Green Chem.*, 2014, **16**, 516–547.

33 E. Ahmad, M. I. Alam, K. Pant and M. A. Haider, *Green Chem.*, 2016, **18**, 4804–4823.

34 P. P. Upare, Y. K. Hwang and D. W. Hwang, *Green Chem.*, 2018, **20**, 879–885.

35 W. Ouyang, D. Zhao, Y. Wang, A. M. Balu, C. Len and R. Luque, *ACS Sustainable Chem. Eng.*, 2018, **6**, 6746–6752.

36 D. Zhao, Y. Wang, F. Delbecq and C. Len, *Mol. Catal.*, 2019, **475**, 110456.

37 R. Mariscal, P. Maireles-Torres, M. Ojeda, I. Sádaba and M. L. Granados, *Energy Environ. Sci.*, 2016, **9**, 1144–1189.

38 P. Demma Carà, R. Ciriminna, N. Shiju, G. Rothenberg and M. Pagliaro, *ChemSusChem*, 2014, **7**, 835–840.

39 P. Zhai, G. Lv, Z. Cai, Y. Zhu, H. Li, X. Zhang and F. Wang, *ChemistrySelect*, 2019, **4**, 3940–3947.

40 D. Ding, J. Xi, J. Wang, X. Liu, G. Lu and Y. Wang, *Green Chem.*, 2015, **17**, 4037–4044.

41 L. Ye, Y. Han, H. Bai and X. Lu, *ACS Sustainable Chem. Eng.*, 2020, **8**, 7403–7413.

42 P. Manjunathan, V. S. Marakatti, P. Chandra, A. B. Kulal, S. B. Umbarkar, R. Ravishankar and G. V. Shanbhag, *Catal. Today*, 2018, **309**, 61–76.

43 Y. Sun, P. Afanasiev, M. Vrinat and G. Coudurier, *J. Mater. Chem.*, 2000, **10**, 2320–2324.

44 W. Liu, Z. Song, T. Ikegawa, H. Nishiguchi, T. Ishihara and Y. Takita, *Mater. Lett.*, 2004, **58**, 3328–3331.

45 D. Spielbauer, G. Mekhemer, T. Riemer, M. Zaki and H. Knözinger, *J. Phys. Chem. B*, 1997, **101**, 4681–4688.

46 A. Sinhamahapatra, N. Sutradhar, B. Roy, A. Tarafdar, H. C. Bajaj and A. B. Panda, *Appl. Catal., A*, 2010, **385**, 22–30.

47 X. Feng, Z. Cui, K. Ji, C. Shen and T. Tan, *Appl. Catal., B*, 2019, **259**, 118108.

48 Y.-B. Huang, T. Yang, M.-C. Zhou, H. Pan and Y. Fu, *Green Chem.*, 2016, **18**, 1516–1523.

49 A. Chappaz, J. Lai, K. De Oliveira Vigier, D. Morvan, R. Wischert, M. Corbet, B. Doumert, X. Trivelli, A. Liebens and F. O. Jérôme, *ACS Sustainable Chem. Eng.*, 2018, **6**, 4405–4411.

50 J. P. Lange, W. D. van de Graaf and R. J. Haan, *ChemSusChem*, 2009, **2**, 437–441.

51 D. Zhao, P. Prinsen, Y. Wang, W. Ouyang, F. Delbecq, C. Len and R. Luque, *ACS Sustainable Chem. Eng.*, 2018, **6**, 6901–6909.

52 X.-F. Liu, H. Li, H. Zhang, H. Pan, S. Huang, K.-L. Yang and S. Yang, *RSC Adv.*, 2016, **6**, 90232–90238.

53 P. Neves, S. Lima, M. Pillinger, S. M. Rocha, J. Rocha and A. A. Valente, *Catal. Today*, 2013, **218**, 76–84.

54 P. Neves, M. M. Antunes, P. A. Russo, J. P. Abrantes, S. Lima, A. Fernandes, M. Pillinger, S. M. Rocha, M. F. Ribeiro and A. A. Valente, *Green Chem.*, 2013, **15**, 3367–3376.

55 S. S. Enumula, K. S. Koppadi, V. R. B. Gurram, D. R. Burri and S. R. R. Kamaraju, *Sustainable Energy Fuels*, 2017, **1**, 644–651.

56 G. Wang, Z. Zhang and L. Song, *Green Chem.*, 2014, **16**, 1436–1443.

57 Z. Zhang, K. Dong and Z. Zhao, *ChemSusChem*, 2011, **4**, 112–118.

58 B. Lu, S. An, D. Song, F. Su, X. Yang and Y. Guo, *Green Chem.*, 2015, **17**, 1767–1778.

59 M. S. Tiwari, J. S. Dicks, J. Keogh, V. V. Ranade and H. G. Manyar, *Mol. Catal.*, 2020, **488**, 110918.

60 D. Song, S. An, B. Lu, Y. Guo and J. Leng, *Appl. Catal., B*, 2015, **179**, 445–457.

61 Y. Wang, D. Zhao, K. S. Triantafyllidis, W. Ouyang, R. Luque and C. Len, *Mol. Catal.*, 2020, **480**, 110630.

62 M. S. Tiwari, A. B. Gawade and G. D. Yadav, *Green Chem.*, 2017, **19**, 963–976.

63 X. Jin, T. Oishi, K. Yamaguchi and N. Mizuno, *Chem. – Eur. J.*, 2011, **17**, 1261–1267.

64 Y. Ogasawara, S. Uchida, K. Yamaguchi and N. Mizuno, *Chem. – Eur. J.*, 2009, **15**, 4343–4349.

65 D. R. Lide, *Handbook of Chemistry and Physics*, 2005, p. 474.